Journal of Advanced Research 60 (2024) 127–140

Contents lists available at ScienceDirect

Journal of Advanced Research

journal homepage: www.elsevier.com/locate/jare

Original Article

Modifications of lipid pathways restrict SARS-CoV-2 propagation in human induced pluripotent stem cell-derived 3D airway organoids

Ping-Hsing Tsai [a,b,1], Jun-Ren Sun [c,i,j,1], Yueh Chien [a,1], Man Sheung Chan [a], Winnie Khor [a], Hsin-Chou Yang [d,1], Chih-Heng Huang [c,e,i], Chia-Ni Hsiung [d], Teh-Yang Hwa [d], Yi-Ying Lin [a], Chih-Ling Yeh [a], Mong-Lien Wang [a,f], Yi-Ping Yang [a,f], Yuh-Min Chen [g,h], Fu-Ting Tsai [a], Meng-Shiue Lee [a], Yun-Hsiang Cheng [c,i,j], Shan-Ko Tsai [c], Ping-Cheng Liu [e,k], Shih-Jie Chou [a,b,*], Shih-Hwa Chiou [a,b,*]

[a] Department of Medical Research, Taipei Veterans General Hospital, Taipei 11217, Taiwan
[b] Institute of Pharmacology, School of Medicine, National Yang Ming Chiao Tung University, Taipei 112304, Taiwan
[c] Institute of Preventive Medicine, National Defense Medical Center, Taipei 11217, Taiwan
[d] Institute of Statistical Science, Academia Sinica, Taipei 11529, Taiwan
[e] Department of Microbiology and Immunology, National Defense Medical Center, Taipei 11217, Taiwan
[f] Institute of Food Safety and Health Risk Assessment, School of Pharmaceutical Sciences, National Yang Ming Chiao Tung University, Taipei 112304, Taiwan
[g] Department of Chest Medicine, Taipei Veterans General Hospital, Taipei 112, Taiwan
[h] Faculty of Medicine, School of Medicine, National Yang Ming Chiao Tung University, Taipei 112, Taiwan
[i] Graduate Institute of Medical Science, National Defense Medical Center, Taipei, Taiwan
[j] Department of Physiology and Biophysics, Graduate Institute of Physiology, National Defense Medical Center, Taipei, Taiwan
[k] Graduate Institute of Applied Science and Technology, National Taiwan University of Science and Technology, Taipei, Taiwan

HIGHLIGHTS

- Single-cell RNA sequencing showed that iPSC-AOs exhibition of the genetic profiles highly resembling the genotypes of human airways.
- iPSC-AOs are susceptible to SARS-COV-2 infection and the expressions of S and N proteins after viral infection.
- Bioinformatics analysis indicated the involvement of aberrant enrichment of lipid transport and lipid pathways in infected iPSC-AOs.
- Statin preincubation relocated ACE2, reduced N protein, and limited SARS-CoV-2 infection in iPSC-AOs.
- Lipid modifications consistently inhibited viral entry of various SARS-CoV-2 strains (wild-type, alpha, delta, omicron).

GRAPHICAL ABSTRACT

Human iPSC-derived airway organoids (iPSC-AOs) exhibit cellular heterogenicity resembling the human native airway. Bioinformatics analysis revealed a robust dysregulation in inflammation, lipid-metabolism pathway, and alternative splicing in SARS-CoV-2 infected airway organoids. Manipulating lipid homeostasis using cholesterol-lowering drugs (e.g. Statins) relocated the viral entry receptor angiotensin-converting enzyme-2 (ACE-2), leading to the reduction of SARS-CoV-2 entry and replication.

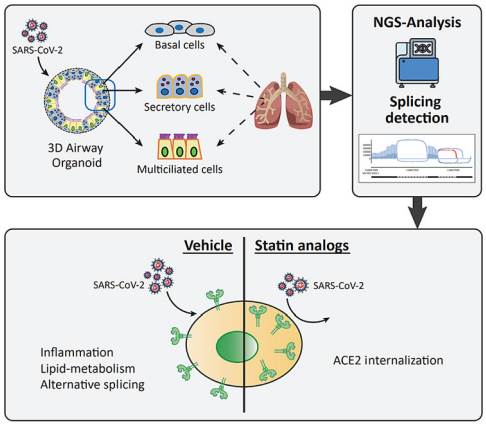

Abbreviations: ACE-2, Angiotensin-converting enzyme-2; COVID-19, Coronavirus disease of 2019; iPSC-AOs, Induced pluripotent stem cell-derived airway organoids; SARS-CoV-2, Severe acute respiratory syndrome coronavirus 2; ScRNAseq, Single-cell sequencing; Fluvastatin and Simvastatin, Statin drugs.

* Corresponding authors.
E-mail addresses: sjchou3@vghtpe.gov.tw (S.-J. Chou), shchiou@vghtpe.gov.tw (S.-H. Chiou).

[1] These authors contributed equally to this work.

https://doi.org/10.1016/j.jare.2023.08.005

ARTICLE INFO

Article history:
Received 4 January 2023
Revised 25 July 2023
Accepted 6 August 2023
Available online 7 August 2023

Keywords:
Severe acute respiratory syndrome coronavirus 2
Induced pluripotent stem cell
Airway organoid
Angiotensin-converting enzyme 2
Single cell RNA-sequencing

ABSTRACT

Background: Modifications of lipid metabolism were closely associated with the manifestations and prognosis of coronavirus disease of 2019 (COVID-19). Pre-existing metabolic conditions exacerbated the severity of severe acute respiratory syndrome coronavirus 2 (SARS-CoV-2) infection while modulations of aberrant lipid metabolisms alleviated the manifestations. To elucidate the underlying mechanisms, an experimental platform that reproduces human respiratory physiology is required.

Methods: Here we generated induced pluripotent stem cell-derived airway organoids (iPSC-AOs) that resemble the human native airway. Single-cell sequencing (ScRNAseq) and microscopic examination verified the cellular heterogeneity and microstructures of iPSC-AOs, respectively. We subjected iPSC-AOs to SARS-CoV-2 infection and investigated the treatment effect of lipid modifiers statin drugs on viral pathogenesis, gene expression, and the intracellular trafficking of the SARS-CoV-2 entry receptor angiotensin-converting enzyme-2 (ACE-2).

Results: In SARS-CoV-2-infected iPSC-AOs, immunofluorescence staining detected the SARS-CoV-2 spike (S) and nucleocapsid (N) proteins and bioinformatics analysis further showed the aberrant enrichment of lipid-associated pathways. In addition, SARS-CoV-2 hijacked the host RNA replication machinery and generated the new isoforms of a high-density lipoprotein constituent apolipoprotein A1 (APOA1) and the virus-scavenging protein deleted in malignant brain tumors 1 (DMBT1). Manipulating lipid homeostasis using cholesterol-lowering drugs (e.g. Statins) relocated the viral entry receptor angiotensin-converting enzyme-2 (ACE-2) and decreased N protein expression, leading to the reduction of SARS-CoV-2 entry and replication. The same lipid modifications suppressed the entry of luciferase-expressing SARS-CoV-2 pseudoviruses containing the S proteins derived from different SARS-CoV-2 variants, i.e. wild-type, alpha, delta, and omicron.

Conclusions: Together, our data demonstrated that modifications of lipid pathways restrict SARS-CoV-2 propagation in the iPSC-AOs, which the inhibition is speculated through the translocation of ACE2 from the cell membrane to the cytosol. Considering the highly frequent mutation and generation of SARS-CoV-2 variants, targeting host metabolisms of cholesterol or other lipids may represent an alternative approach against SARS-CoV-2 infection.

Introduction

In late 2019, the outbreak of the coronavirus disease 2019 (COVID-19) ~~has~~ caused a severe pandemic that led to a considerable amount of confirmed cases (>600 million) and mortality (>6 million). Severe acute respiratory syndrome coronavirus 2 (SARS-CoV-2), the pathogen that caused COVID-19, was first reported in Wuhan Province, China, and was speculated as a zoonotic incident [1]. The virus mainly attacks the human lungs and later spreads to other organ systems, causing life-threatening complications of acute respiratory distress syndrome (ARDS), sepsis, or organ failure. Last year, a newly emerging variant, Omicron [2], further struck the global community with an even more ominous note. Although precautionary measures and vaccination have slowed down the pandemic, scientific communities are still trying to fill in the knowledge gaps about SARS-CoV-2.

To explore the pathological mechanisms of human diseases, numerous cell lines and animal models were used to meet the demand for disease investigations for decades. However, several limitations of the experimental models, including differences in the type of species, native organ architecture, and cellular heterogeneity, largely hinder the full understanding of the diseases. The development of induced pluripotent stem cell (iPSC) technologies not only enables the capabilities of iPSCs for pluripotent differentiation but reproduces the molecular characteristics of the cell donors after defined differentiation [3,4]. In addition, iPSCs can be driven to differentiate into three-dimensional (3D) organ cultures, allowing the structure formation that resembles architecture and functionality in the *in vivo* organs [5]. The resultant iPSC-differentiated 3D architecture, also known as iPSC-derived organoids, can be expanded *in vitro* with the maintenance of genetic integrity after long-term culture. These advantages render iPSC-derived organoids an ideal platform for disease modeling.

The entry of SARS-CoV-2 into the host cells has been well investigated. Through the binding of the SARS-CoV-2 spike (S) protein to the entry receptor angiotensin-converting enzyme 2 (ACE), SARS-CoV-2 is permitted to enter the host cells. After the entry, the virus replicates its genome using nucleocapsid (N) protein and further undergoes virus packaging with the membrane (M) and envelope (E) protein before releasing the new virions into the host bodies [6]. After the outbreak of COVID-19, several attempts have been made to use organoid technologies in virology for modeling SARS-CoV2 infection [7–9]. Relying on the expression of ACE2 as well as the transmembrane protease serine type 2 (TMPRSS2) receptor, iPSC-derived organoids have been shown to be permissive to SARS-CoV-2 infection [10–13]. Owing to the inclusion of cell types and structures resembling human lungs and the expression of lung-specific markers, iPSC-derived lung organoids have been subjected to SARS-CoV-2 infection for testing different therapeutic approaches [11]. Despite the progresses in organoid technologies, iPSC-based disease modeling, and the development of antiviral regimens against COVID-19, the pathomechanisms and effective intervention strategies for SARS-CoV-2 remain generally unclear.

In clinical observations, growing evidence showed that the use of lipid-modulating drugs such as statins is associated with lower disease severity and reduced mortality among COVID-19 patients [14–16]. The beneficial effects of statins on disease outcomes were also observed in several clinical trials, whereas the mechanisms underlying such beneficial effects remain unclear [17]. In the present study, we first attempted to generate iPSC-derived airway organoids (iPSC-AOs) and used microscopic examination and single-cell RNA sequencing (ScRNA-seq) to validate iPSC-AOs that resemble human lungs in phenotypic features, cellular heterogeneity, and gene expression patterns. The detection of S and N proteins after viral infection supported that iPSC-AOs are permissive to SARS-CoV-2 entry and replication. Bioinformatics approaches

revealed a robust dysregulation in lipid-related pathways in infected iPSC-AOs. We next treated iPSC-AOs with statin drugs and evaluated the effect of manipulating lipid homeostasis on the trafficking of ACE2, the SARS-CoV-2 entry receptor, as the infection and replication of SARS-CoV-2 in iPSC-AOs. Furthermore, we compared the effect of modifying lipid homeostasis and examined whether this intervention restricted SARS-CoV-2 infection among iPSC-AOs exposed to different virus variants, i.e. wild-type, alpha, delta, and omicron.

Materials and methods

General mammalian cell culture conditions

The HEK293-ACE2 cell line constitutively expresses human Angiotensin-converting enzyme 2 (ACE2) by transduction of ACE2 into HEK293 cell [18]. The HEK293-ACE2 cell line was cultured and maintained in Dulbecco's modified Eagle's medium (DMEM) (Gibco), supplemented with 10% (v/v) fetal bovine serum (Gibco) and 1 × penicillin–streptomycin (Gibco). Cells were passaged at 80% confluency using 0.25% trypsin. For hiPSC maintenance, the cell colonies were passaged as single cells using Versene (Gibco), and cultured on Geltrex (Corning)-coated culture dish in commercially available StemFlex medium (Gibco), supplemented with 10 μM ROCK inhibitor during the first day of subculture. All cell types were maintained and cultured at 37 ℃ with 5% CO_2.

Generation of airway organoids

Human iPSCs were stepwise differentiated into airway organoids (iPSC-AOs), following the protocol reported previously [19]. Briefly, 2 × 10^6 of iPSCs were cultured in Geltrex-coated 6-well plates with StemFlex medium 24 h prior to being induced into definitive endoderm with STEMdiff Definitive Endoderm Kit (Stem Cell Technologies) for 72 h. At this stage, the cells were dissociated and cultured as small clumps in the Geltrex-coated 6-well plate at the ratio of 1:7 in a complete serum-free differentiation medium, cSFDM (IMDM, Ham's F12, B27 Supplement, N2 Supplement, 0.1% bovine serum albumin Fraction V, monothioglycerol, Glutamax, L-ascorbic acid, and Pen/Strep), supplemented with 10 μM SB431542 and 2 μM Dorsomorphin for 72 h to induce the cells towards anterior foregut endoderm development. The cells were cultured for another 9–11 days (D14–D16) in cSFDM containing 3 μM CHIR99021, 10 ng/ml rhBMP4, and 100 nM retinoic acid for lung epithelial progenitor cells induction. Later, cells expressing $CD47^{high}/CD26^{low}$ markers were sorted using BD FACSAria™ III Cell Sorter (BD Biosciences) for further differentiation into the 3D airway organoids. The sorted cells were maintained in the Matrigel (Corning) at a seeding density of 200 cells/μL of Matrigel and fed with airway differentiation medium (ADM): cSFDM medium, supplemented with 0.1 mM 8-Bromoadenosine 3′, 5′-cyclic adenosine monophosphate, 250 ng/ml recombinant human fibroblast growth factor 2, 100 ng/ml recombinant human fibroblast growth factor 10, 50 nM dexamethasone, 0.1 mM 3-Isobutyl-1-methylxanthine, and 10 μM Rock inhibitor. DAPT, a Notch signaling inhibitor was added post two weeks of sorting to induce ciliary motility. The organoids can be dissociated into single cells for further passaging or cryopreservation.

Immunofluorescence staining

Immunofluorescence (IF) staining of the monolayer-cultured HEK293-ACE2 cells was performed using the general protocol. Briefly, cells were fixed and permeabilized with 4% paraformaldehyde (PFA) and Trixton-X 100, respectively before being incubated with primary antibodies overnight at 4℃. On the next day, cells were washed three times with phosphate-buffered saline (PBS), then incubated with secondary antibodies and counterstained with DAPI before visualization. For whole-organoid IF staining, the 3D airway organoids were isolated from Matrigel extracellular matrix using Dispase (Corning) and fixed with 4% PFA in the 8-well chamber slides (Merck Millipore). Next, the organoids were permeabilized and blocked in blocking buffer (5% BSA + 0.5% Triton X-100 in 1 × PBS) for 2 h, before being incubated with primary antibodies overnight at 4℃. Similarly, secondary antibodies and DAPI counterstain were given the next day before analysis. All IF images were taken with a confocal laser scanning microscope (FLUOVIEW FV3000, Olympus). All primary and secondary antibodies used in the IF analyses are listed in **Supplementary Table 1**.

10x Single-cell RNA sequencing of airway organoid

The differentiated airway organoids were prepared with 10x Genomics Single Cell 3′ v3 Reagent Kit as our previous study described [20]. Briefly, we carefully dissociated the organoid with trypsin and washed it twice with commercial PBS plus 0.04% BSA (Sigma). We then resuspended the dissociated cells in PBS plus 0.04% BSA and checked the viability by Trypan blue staining (Thermo Fisher). After confirming the viability higher than 80 %, we applied the 6,672 cells for single-cell cDNA preparation as manufacturing instruction. After amplifying the cDNA with 12-cycle PCR, we used SPRIselect beads (Beckman) to purify the suitable-length DNA. The quality was confirmed by Bioanalyzer (Agilent Technologies) and determined their concentration. We prepared the cDNA library according to manufacturing instructions and sequenced it with Illumine NovaSeq 6000.

Western-blotting

The total protein of cells and organoids from different experiment groups were extracted using the general western blotting protocol and quantified by Bradford assay. An equal amount of protein lysate (30 μg) was separated by the SDS-PAGE system and transferred to polyvinylidene difluoride membranes. For immunoblotting, the membranes were blocked with 5% non-fat milk in PBS/0.1% Tween 20 (PBST) before being incubated overnight at 4 °C with primary antibodies of interest. The membranes were washed three times with PBST the next day to remove excessive antibodies, followed by 1 h incubation at room temperature (RT) with species-specific secondary antibodies conjugated with horseradish peroxidase (HRP). Finally, membranes were exposed to chemiluminescent HRP detection reagents (Millipore) and the blots were developed using the X-ray film in the dark room. All primary and secondary antibodies are listed in **Supplementary Table 1**.

SARS-CoV-2 luciferase assay

HEK293-ACE2 cells were seeded into a white opaque 96-well plate (Corning). The next day, we pretreated cells with 0, 5, and 10 μM of Remdesivir, Fluvastatin, and Simvastatin for 24 h, respectively. After 24 h, we replaced the medium with the phenol-red free culture medium containing one MOI virus (SARS-CoV-2-Nluc). After 48 h post-infection, we added luciferase substrates (Promega) to 50 μL cell lysate from each well. The luciferase activity was normalized with the luciferase signals of the mock group (set as 100%). All experiments were performed with technical duplicates.

Quantitative RT-PCR (qPCR)

Total RNA in the cells was extracted using Trizol (Invitrogen) according to the manufacturer's protocol, and 1 μg of the RNA was reverse transcribed into cDNA. The qPCR was performed using the Applied Biosystems QuantStudio 5 Real-Time PCR System (Thermo Fisher Scientific). The cycling conditions were as follows: polymerase activation at 95 °C for 2 min, followed by 40 cycles of denaturation at 95 °C for 10 s, and annealing at 60 °C for 30 s.

GFP-Forward: CTACCCCGACCACATGAAGC; GFP-Reverse: AAGAAGATGGTGCGCTCCTG.

Transmission electron microscopy (TEM)

Organoids were collected and immersed in a fixative buffer containing 2% PFA (Electron Microscopy Science, PA, USA) and 2.5% glutaraldehyde (Electron Microscopy Science, PA, USA) in 0.1 M PBS overnight. The fixed organoids were washed with PBS three times and fixed in 1% osmium tetroxide (OsO_4, Electron Microscopy Science, PA, USA) for 2 h at RT for further dehydration. Dehydration was operated by sequential changing the alcohol (Merck) concentration from 30%, 50%, 70%, 80%, 85%, 90%, 95%, and 100%, followed by replacement with propylene oxide (Merck) and Spurr's epoxy (Electron Microscopy Science, PA, USA). By gradually changing the concentration of Spurr's epoxy, the samples were finally infiltrated with pure Spurr's epoxy overnight. The samples were carefully embedded into separate BEEM capsules (Electron Microscopy Science) and cured for 72 h at 70℃ before sectioning using an ultramicrotome (Leica EM UC7, Leica Microsystems). The sections on the copper grids were stained with 2% uranyl acetate (Electron Microscopy Science, PA, USA) and 2.5% lead citrate (Electron Microscopy Science, PA, USA) and observed in a TEM (JEM-1400plus, 80 kV, JEOL Ltd.). Images were acquired by the CCD camera on TEM with identical magnification.

Rna-seq sequencing, data processing, and data analysis

Total RNA of the uninfected and virus-infected organoids were harvested followed by mRNA isolation using Oligo$(dT)_{25}$ (Thermo Fisher Scientific) following the manufacturer's instruction. Purified and fragmented RNA (with an approximate average length of 200 bp) were used in first-strand and second-strand cDNA synthesis followed by 3′ends polyadenylation and adaptor ligation before final enrichment, according to the instructions of NEBNext Ultra RNA Library Prep Kit for Illumina (New England Biolabs). The quality of the purified library products was evaluated using the Agilent 2200 TapeStation system (Agilent) and Qubit 2.0 fluorometer (Life Technologies). RNA sequence quality of FASTQ files was checked using FastQC [21]. Leftover ~~of~~ adapter sequences and poor-quality bases at read ends from every read were trimmed off by using Trimmomatic v.0.39 [22] before the reads were mapped to the reference genome. The reference genome was built by combining the reference genomes of homo sapiens (GRCh38, https://www.ncbi.nlm.nih.gov/assembly/GCF_000001405.39/) and SARS-CoV-2 (human/TWN/CGMH-CGU-04/2020; GenBank number: MT370517). Total RNA-seq reads from sequencing the lung organoid samples were mapped to the reference genome by using STAR 2.7.3a [23] with permissive parameters for noncanonical splicing [24,25]. Reads that mapped equally well to multiple genomic regions were removed. The mapping and generation of count tables were performed using Featurecounts [26]. Normalization and identification of differentially expressed genes were processed using the R package DESeq2 [27]. Estimated effect sizes and p-values of differentially expressed genes were displayed in a volcano plot by using the R package ggplot2 [28]. Gene clusters were constructed by using GAP [29], where the Pearson correlation coefficient was used as a proximity to measure the between-gene association. An average linkage hierarchical clustering dendrogram with Pearson correlation proximity was constructed. The nomenclature of the gene clusters was assigned through a gene ontology enrichment analysis [30,31]. All information on used software is listed in Table 1.

Functional enrichment analysis

DEGs were classified into multiple subgroups according to the temporal profiles of gene expression at mock, 24 h, and 96 h. A GO enrichment analysis was carried out in each subgroup using the R package *goseq* [32]. The GO terms enriched by the identified DEGs were further grouped into several clusters by using *rrvgo* [33], and then cluster names were assigned, and GO networks were analyzed by the website *REVIGO* [34] and plotted using *visNetwork*

Table 1
The used software and algorithms in the study.

Software	Ref.	Website
fastQC v.0.11.8	[21]	https://www.bioinformatics.babraham.ac.uk/projects/fastqc/
Trimmomatic v.0.39	[22]	https://www.usadellab.org/cms/index.php?page = trimmomatic
STAR 2.7.1a	[23]	https://hbctraining.github.io/Intro-to-rnaseq-hpc-O2/lessons/03_alignment.html
Featurecounts	[26]	https://subread.sourceforge.net/
DeSeq2	[27]	https://bioconductor.org/packages/release/bioc/html/DESeq2.html
GAP	[29]	https://gap.stat.sinica.edu.tw/Software/index.htm
GRCh38	–	https://www.ncbi.nlm.nih.gov/assembly/GCF_000001405.39/
SARS-CoV-2	[78]	https://www.ncbi.nlm.nih.gov/nuccore/MT370517
GO analysis	[30,31]	https://geneontology.org/
goseq v1.46.10	[32]	https://doi.org/10.18129/B9.bioc.goseq
rrvgo v1.6.0	[33]	https://doi.org/10.18129/B9.bioc.rrvgo
IMPaLA v13	[37]	https://impala.molgen.mpg.de/
KEGG database	[79–81]	https://www.genome.jp/kegg/kegg1.html
pathview v1.34.0	[82]	https://doi.org/10.18129/B9.bioc.pathview
HISAT2 v2.2.1	[40]	https://daehwankimlab.github.io/hisat2/
regtools v0.5.2	[42]	https://github.com/griffithlab/regtools
StringTie v2.1.5	[43]	https://ccb.jhu.edu/software/stringtie/
ballgown v2.24.0	[44]	https://doi.org/10.18129/B9.bioc.ballgown
IsoformSwitchAnalyzeR v1.14.1	[45,46]	https://doi.org/10.18129/B9.bioc.IsoformSwitchAnalyzeR
ggsashimi v1.1.5	[47]	https://github.com/guigolab/ggsashimi
ggplot2 v3.3.5	[28]	https://ggplot2.tidyverse.org/
visNetwork v2.1.0	[35]	https://CRAN.R-project.org/package = visNetwork
EnrichR	[38]	https://maayanlab.cloud/Enrichr/#

[35]. Combining the identified DEGs in this study and metabolites that were associated with the SARS-CoV-2 infection [36], an integrative pathway analysis was conducted by using *IMPaLA* [37]. EnrichR [38] was used to identify the Gene Ontology (GO) for the Biological process. Log2 expression of each gene of more than three were selected in the EnrichR. Alternatively, the Cytoscape package ClueGO [39] was also used to map the over-presentative GO term. EnrichR can obtain the P-value and q-value by the Fisher exact test. The GO terms with the q-value < 0.05 were considered statistically significant.

Isoform detection

Trimmed RNA-seq reads were mapped to the reference genome by using *HISAT2* [40] based on an analysis protocol [41]. All junctions were extracted from the alignments using *regtools* [42]. Junctions with differential expressions were identified in the pairwise comparisons (mock, 24 h, and 96 h). Isoform assembly was conducted by using *StringTie* [43], *ballgown* [44], and the R package *IsoformSwitchAnalyzeR* [45,46]. Assembled isoforms were ranked and sorted according to the coverages of differential junctions. The top 50 isoforms with the highest coverages were visualized in Sashimi plots by using *ggsashimi* [47].

Cell viability assay

To determine the possible cytotoxicity effect of Statin on the mammalian cells, we performed cell viability assay using cell counting kit-8 (CCK-8) (Sigma Aldrich). HEK293-ACE2 cells were plated in a 96-well plate and later incubated with a range of concentrations of Statin (1, 2, 5, 10, 20, and 50 μM), and meanwhile negative control groups with PBS for 48 h at 37℃ with 5% CO_2. For the assay, 10 μL of CCK-8 solution was added to each well of the plate and incubated for 2 h before being measured using a microplate reader at an absorbance of 450 nm.

SARS-CoV-2 and pseudovirus infection with drugs treatment

All the experiments with infectious SARS-CoV-2 were employed in appropriate biosafety level (BSL) 3 or BSL 4 laboratories, at the Institute of Preventive Medicine (IPM). SARS-CoV-2 was obtained from Taiwan Centers for Disease Control. The SARS-CoV-2 pseudovirus was purchased from National RNAi Core Facility at Academia Sinica in Taiwan. To evaluate the antiviral efficacy of remdesivir and Statin, HEK293-ACE2 cells or airway organoids were pre-treated with remdesivir or Statin analogs at the indicated doses, respectively. After drug treatment, the cells were infected with pseudovirus or SARS-CoV-2 (one MOI) for 1 h and the viruses were removed and cultured for 48 h. The viruses were tittered using a plaque assay on Vero E6 cells. For GFP- or luciferase-conjugated pseudovirus, cells were either viewed under a confocal microscope or subjected to luciferase activity assay by following the manufacturer's instructions. The Remdesivir, Fluvastatin (Sigma-Aldrich), and Simvastatin (Sigma-Aldrich) administration were treated prior to 24 h of infection. For SARS-CoV-2 infection groups, organoids were lysed for western immunoblotting or fixed for subsequent IF staining.

Statistical analysis

If not specified, all bioassays were performed in triplicates and expressed as mean ± S.E.M. The average data and their respective standard deviation were obtained using Microsoft Excel or GraphPad Prism version 7.0 software. For the comparison of two groups, a *t*-test (paired or unpaired) was performed by Prism. For the comparison of three or more groups, one-way ANOVA analysis of variance with an appropriate multiple comparisons test was performed by Prism, $P < 0.05$ was considered statistically significant.

Results

Human iPSC-AOs express human airway markers and the machinery for SARS-CoV-2 infection

The pluripotency property grants iPSCs the ability to differentiate into all human cell lineages. Considering the human lung as the primary target organ of SARS-CoV-2, we induced the differentiation of human iPSCs into 3D airway organoids (iPSC-AOs) **(**Fig. 1**A & B)** [19]. Immunofluorescence staining detected the various cell populations expressing airway markers of basal (KRT5 +), secretory (SCGB3A2 +), and ciliated (Act-α-TUB +) cells in iPSC-AOs **(**Fig. 1**C)**. Single-cell transcriptome analysis further supported our findings, revealing genes that represent five distinct clusters of multiciliated cells (CDK1), secretory cells (CEACAM6), basal cells (KRT17), alveolar epithelial type 1 cells (OBSL1), and alveolar epithelial type 2 cells (TTYH1) **(**Fig. 1**D)**. These findings are consistent with that of human lung transcriptomes analyzed using Single-cell RNA-sequencing (ScRNAseq) in previous studies [48,49]. Upon microscopic examination, we also observed beating cilia on the apical layer of the iPSC-AOs after 30 days of differentiation, resembling the native airway mucociliary movement (Video S1). Using ScRNAseq and immuno-blotting, we further detected ACE2 expression at both gene and protein levels, respectively **(**Fig. 1**E & F)**. To validate whether iPSC-AOs are permissive to SARS-CoV-2 infection, we subjected iPSC-AOs to the infection using green fluorescence protein (GFP)-tagged SARS-CoV-2 pseudovirus. The SARS-CoV-2 pseudovirus was produced by the transfection of the HEK 293 T cells with a lentiviral backbone that encodes a fluorescent reporter protein and the SARS-CoV-2 S protein [50,51]. After the exposure to SARS-CoV-2 pseudovirus, strong GFP signals were detected within the iPSC-AOs using immunofluorescence staining **(**Fig. 1**G)**. Quantitative real-time polymerase chain reaction (qPCR) also showed high expression of GFP signals in the iPSC-AOs after ~~the~~ exposure to SARS-CoV-2 pseudovirus **(**Fig. 1**H)**. These findings suggested that iPSC-AOs recapitulate the cellular heterogeneity and gene expression patterns of the human native airway and may act as a feasible platform for SARS-CoV-2 infection.

iPSC-AOs are vulnerable to SARS-CoV-2 infection

Owing to the susceptibility of iPSC-AOs to SARS-CoV-2 pseudovirus, we next infected the iPSC-AOs with wild-type SARS-CoV-2 virus (MOI = 1) for different time courses in subsequent experiments **(**Fig. 2**A)**. Time-point imaging indicated the mock iPSC-AOs self-organized and expanded time-dependently, whereas the post-infection iPSC-AOs lost the ability for volume expansion over time **(**Fig. 2**B, Video S2)**. After exposure to wild-type SARS-CoV-2 and iPSC-AO harvesting~~, immunoblotting,~~ and immunofluorescence ~~both~~ showed increased expression of the SARS-CoV-2 spike (S) and nucleocapsid (N) proteins **(**Fig. 2**C & D)**, indicating the SARS-CoV-2 entry and replication, respectively. Notably, ACE2 expression was dramatically reduced at 96 h post-infection. These findings suggested the self-defense of iPSC-AOs against SARS-CoV-2 infection, consistent with clinical observations among COVID-19 patients [52]. We further used transmission electron microscopy (TEM) to capture SARS-CoV-2 propagation within iPSC-AOs. The presence of the SARS-CoV-2 virions (indicated by red arrows) and the virus replicative structures (indicated by green arrows) provided evidence demonstrating the viral entry and replication within this iPSC-derived 3D platform **(**Fig. 2**D)**. Collectively,

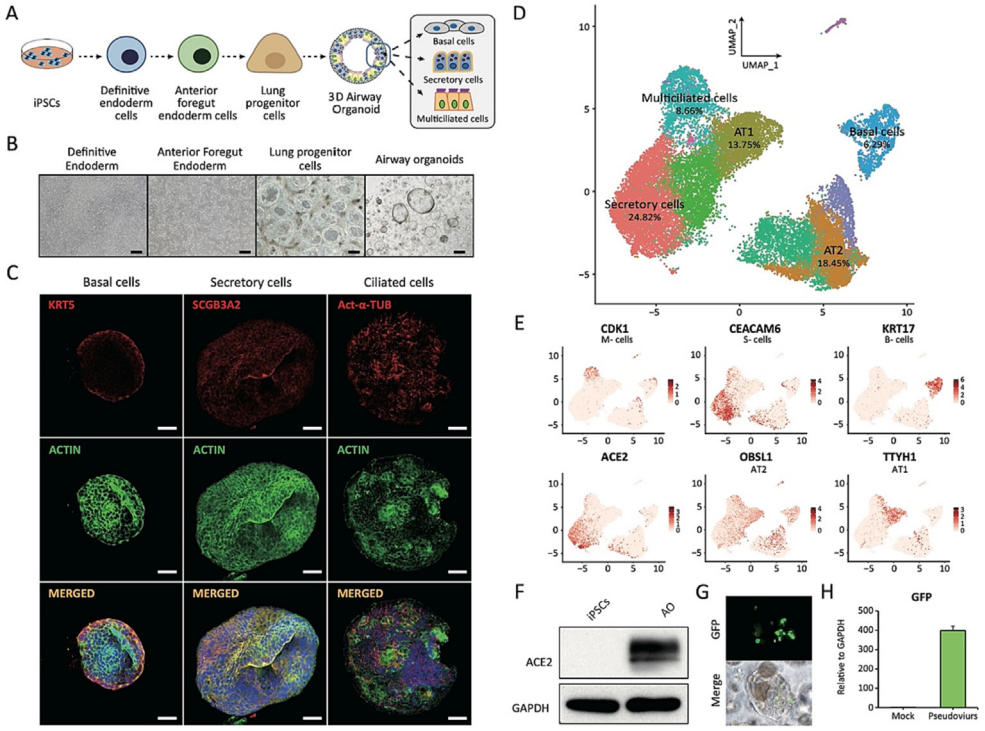

Fig. 1. Ipsc-derived airway organoids (ao) exhibit ace2 expression and vulnerable to sars-cov-2 pseudovirus infection. (A) Schematic illustration of the differentiation process of iPSCs to AO. (B) Brightfield image of the iPSC-derived AO at different stages of differentiation spanning ≧ 30 days. Scale bar = 200 μm. (C) Immunofluorescence staining of AO showed marker expression of basal cell (KRT5), secretory cell (SCGB3A2 and CFTR), and ciliated cell (Act-α-TUB). Nuclei and cellular actin filaments were counterstained with DAPI (blue) and ACTIN (green), respectively. Scale bar = 20 μm. (D) Cluster map showing the assigned identity for each airway component (Multiciliated, Secretory, Basal, AT1, and AT2 cells). (E) t-SNE projection showing major airway marker CDK1, CEACAM6, KRT17, OBSL1, TTYH1, and ACE2 expressions in the AO. (F) Immunoblotting analysis showed high ACE2 protein expression in iPSC-derived AO. (G) iPSC-derived AO expressed GFP signals after 48 h infection with GFP-conjugated SARS-CoV-2 pseudovirus. Scale bar = 100 μm. (H) Quantitative real-time PCR analysis showed increased mRNA expression level of GFP; n = 3. (For interpretation of the references to colour in this figure legend, the reader is referred to the web version of this article.)

these data indicated that iPSC-AOs are vulnerable to SARS-CoV-2 infection and serve as an ideal platform for investigating the pathomechanisms of COVID-19.

Differentially expressed gene expression in iPSC-AOs in response to SARS-CoV-2 infection

We performed RNA-sequencing (RNAseq) to profile differential gene expression in the iPSC-AOs after SARS-CoV-2 infection. The detailed flow chart of sequencing analysis is shown in Fig. 3**A.** After quality control and pre-processing of RNAseq data, we performed differential expression gene analysis. In iPSC-AOs, we identified 1,643 differentially expressed genes (DEGs) after 24-hour infection (1,122 upregulated and 521 downregulated genes) and 1,282 DEGs after 96-hour infection (888 upregulated and 394 downregulated genes), compared to the uninfected iPSC-AOs. In infected iPSC-AOs at 24 h post-infection, Egl-9 Family Hypoxia Inducible Factor 3 (EGLN3) was the most upregulated gene (FDR adjusted p-value = 9.32×10^{-63}) with a 3.97-fold upregulation. Transcription factor 21 (TCF21) was the most decreased gene (FDR adjusted p-value = 4.47×10^{-43}) with a 3.36-fold downregulation (Left subpanel in Fig. 3B). For iPSC-AOs at 96 h post-infection, cyclin and CBS domain divalent metal cation transport mediator 1 (CNNM1) were the most significantly upregulated gene (p-value = 7.83×10^{-25} 3.70×10^{-29}) with a 4.59-fold increase, while periostin (POSTN) was the most significantly decreased gene (FDR adjusted p-value = 4.07×10^{-23}) with a 4.00-fold decrease in gene expression (Right subpanel in Fig. 3**B**). The majority of identified DEGs were different between iPSC-AOs with 24-hour infection and 96-hour infection. Among these DEGs, only 10.5% of DEGs (279 DEGs) were overlapped, illustrating the dramatical differential transcriptomic changes after short-term exposure (24 h) and prolonged exposure (96 h) to SARS-CoV-2 infection (Fig. 3**C**). To reveal the participating biological processes (BPs) contributed by these DEGs, we first performed the gene ontology (GO) analysis of these dysregulated DEGs in the infected iPSC-AOs after 24-hour infection. The GO analysis revealed the involvement of several typical biological responses of virus infection, such as proteolysis (GO:0006508), response to virus (GO:0009615), inflammatory response (GO:0006954), and acute phase response (GO:0006953), resembling the manifestations of the human physiological environment in response to virus infection. Remarkably, GO analysis also showed the involvement of lipid transport (GO:0006869) and lipid metabolic processes (GO:0006629) in response to SARS-CoV-2 infection (Fig. 3**D**). Transcription factors of the same signaling usually have a similar expression pattern due to sharing the same promoter or the control of the same regulatory loops. For a more precise understanding of the interaction networks, we conducted a similarity matrix to capture the transcription pattern and mapped the major effectors. According to the transcriptional profiles of DEGs in iPSC-AOs after 24 h infection, we classified the transcriptional profiles into eleven groups, including response to chemotaxis, development differentiation, proliferation cell regulation, death cell process apoptotic, transport cell migration lipid, regulation negative growth, homeostasis process homeostatic maintenance lipid, immune regulation, etc. (Fig. 3**E**). Among the processes, GO terms related to chemotaxis response, cell metabolism, lipid transport, and apoptosis were significant, especially in iPSC-AOs after 24 h infection (Fig. 3**F**). Due to the loss of expansion ability (Fig. 2**B**) and the significantly upregulated pathways related

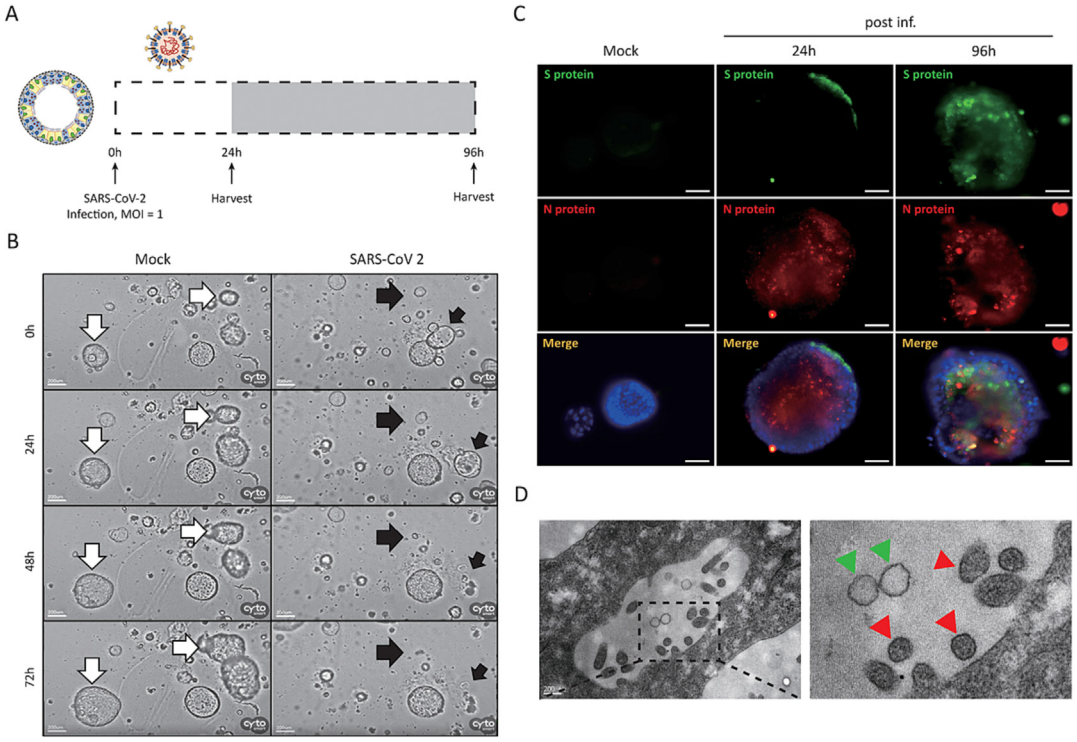

Fig. 2. Human iPSC-derived airway organoids (iPSC-AO) are vulnerable to SARS-CoV-2 infection. (A) Schematic illustration of SARS-CoV-2 virus infection in AO. **(B)** Time-lapse images of SARS-CoV-2-infected AO. The white arrow indicated the same organoid in the mock group, and black arrow indicated the same organoids in the infection group. **(C)** Immunofluorescence staining of N protein and S protein in SARS-CoV-2-infected AO. Nuclei were counterstained with DAPI (blue). Scale bar = 20 μm. **(D)** Transmission electron microscope analysis detected successful SARS-CoV-2 virus infection in AO, indicated by arrow. Scale bar = 200 nm. (For interpretation of the references to colour in this figure legend, the reader is referred to the web version of this article.)

to cellular death response (Fig. 3**D, 3F, and S3**) in iPSC-AOs at the 96 h post-infection, we then focused on the infected iPSC-AOs after 24 h infection and investigated the changes of lipid pathways in response to SARS-CoV-2 infection in subsequent experiments.

Enrichment of lipid-associated pathways in SARS-CoV-2-infected iPSC-AOs

To assess whole transcriptional changes during SARS-CoV-2 infection, we harvested the RNA from the SARS-CoV-2-infected iPSC-AOs at 24 h and 96 h post-infection and compared the gene expression with that in uninfected iPSC-AOs. We carefully performed a quality control (QC) validation and trimmed the raw reads for precise transcriptional quantification (Fig. 4**A**). Briefly, we aligned the raw reads to the SARS-CoV-2 genome, cleaned the viral RNA, and aligned the remaining reads to the human genome. We counted and normalized the alignments by cufflinks and DESeq2, respectively, and eventually obtained the DEGs from the analysis pipeline. According to the temporal dynamic patterns of these identified DEGs, we classified these DEGs into five categories and used GO enrichment analysis and text mining cluster analysis to identify their activated biological processes (BPs). The top three prominent GOs of each category are shown in Fig. 4**B**. The first group was associated with cell response to stress, including defense response, immune response, and cellular response to chemical stimuli. The second group was associated with cell replication, including cell cycle, nuclear DNA replication, and epithelial cell proliferation. The last group was associated with lipid metabolism, including lipid metabolic process, regulation of lipoprotein lipase activity, response to lipid, etc. Together, we found substantial changes in gene expression levels and the critical roles of immune, inflammatory, and defense responses to SARS-CoV-2 infection in host cells, particularly at the early stage of viral infection. Under the attack by SARS-CoV-2, it has been shown that the host cells eliminated foreign substances through the release of defense signals damage-associated molecular patterns (DAMPs), such as interleukins and interferon families. Overstimulation by these signals was shown to result in inflammation and cell death [53–55]. Remarkably, GO enrichment analysis indicated that lipid metabolism was the predominant function during SARS-CoV-2 infection, implying that aberrant regulation of lipid pathways may be involved in SARS-CoV-2 propagation (Fig. 4**B**). Extensive studies have shown that cholesterol facilitates the production of infectious particles in viruses such as Hepatitis C and flavivirus [56,57]. At the early stage of SARS-CoV-2 infection in iPSC-AOs, significantly upregulated genes are associated with positive regulation of cholesterol esterification, plasma lipoprotein particle remodeling, and regulation of lipoprotein lipase activity, suggesting that SARS-CoV-2 modulates the host lipid metabolism to meet the demand of viral entry and formation of replication vesicles. Genes related to response to lipid and response to lipopolysaccharide were enriched during prolonged viral infection, further emphasizing the essential roles of lipids in the SARS-CoV-2 life cycle (Fig. 4**B**). Alternatively, we calculated all DEGs with proportion statics with the ClueGO software. The PiePlot of enriched GOs showed that plasma lipoprotein particle remodeling has a dominant proportion (34.48%). Meanwhile, the positive regulation of monocyte aggregation (17.24%) and regulation of neutrophil activation (13.79%) resembled the typical lung epithelial cell response in the human tissue under viral infection (Fig. 4**C**). Among these major groups, we found that multiple GOs closely interacted with each other and represented a vivid pathological response *in vitro* (Fig. 4**D**). To identify the canonical pathways within the infected iPSC-AOs, we applied the DEGs into Bioplant 2019 database. The EnrichR analysis showed that the Statin pathway, chylomicron-mediated lipid transport, and lipoprotein metabolism

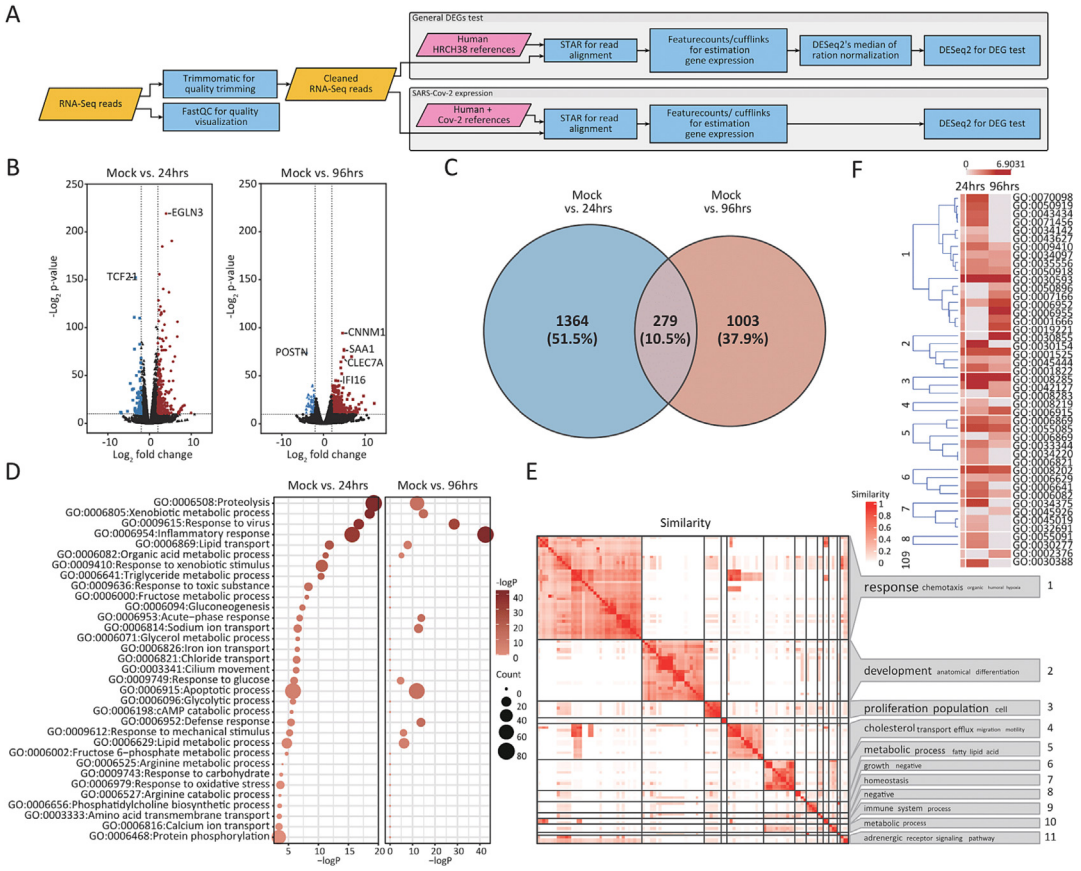

Fig. 3. Next-generation sequencing analysis of SARS-CoV-2 infection in airway organoid. (A) Flowchart of RNA sequencing data analysis. The major analysis components consist of data quality control and preprocessing, differential expression gene analysis, gene ontology and pathway analysis, and isoform detection and splice junction analysis. **(B)** The left-hand-side and right-hand-side volcano plots display the results in a comparison analysis between the mock sample and SARS-CoV-2 infected sample at 24 h and 96 h, respectively. Volcano plot representing the DEGs satisfying the criteria of log 2 (fold-change) value > 2 or < -2 and p < 0.05. Red and green symbols indicate significantly upregulated and downregulated genes, respectively. **(C)** Venn diagram shows that 279 genes were commonly identified at 24 h- and 96 h-exposure to viral infection. Purple circle indicates the number of DEGs identified at 24 h exposure to viral infection compared to the mock sample; Orange circle indicates the number of DEGs identified at 96 h exposure to viral infection compared to the mock sample. **(D)** The bubble plot showed the gene ontology of the 24 h and 96 h infection-affected genes. **(E)** The heatmap of the semantic similarity matrix from top-ranking random GO terms in 24 h infection-affected group. **(F)** Heatmap presents the significance of biological processes in the infected cells after 24 h SARS-CoV-2 infection, which are compared to that after 96 h SARS-CoV-2 infection. (For interpretation of the references to colour in this figure legend, the reader is referred to the web version of this article.)

were significantly upregulated (P value = 4.10×10^{-5}, 1.97×10^{-4}, and 3.68×10^{-4}, respectively). To identify which pathway is dominant, we then used EnrichR to calculate the Odds ratio. The scattering plot showed that the Statin pathway has the strongest association with exposure to SARS-CoV2 and the consequence of viral infection (Fig. 4**E & F**). To examine whether these associated genes were also highly expressed upon SARS-CoV-2 infection, we analyzed the transcripts levels of these associated genes in the results of RNAseq. Overall, the lipoprotein-associated genes, including CETP, LPL, APOC3, APOA1, APOA4, and APOB, were abundant and significantly upregulated. Meanwhile, the interferon-alpha/beta signalings were also significantly enriched (Fig. 4**G**). Taken together, our findings demonstrated that the lipid-associated pathways were significantly enriched in response to SARS-CoV-2 infection in iPSC-AOs.

SARS-CoV-2 promotes alternative splicing to generate isoforms of APOA1 and DMBT1

Alternative splicing is a frequent regulation that can adjust the detailed protein–protein interaction or complex assembly by generating the transcripts of different mature mRNA splice isoforms [58]. COVID-19 has been known to induce exacerbated pulmonary and systemic inflammation [59]. Although clinical manifestations are generally similar, some of the symptoms and complications among COVID-19 patients were distinct and diverse, which may be probably the consequences of alternative splicing [60]. Recent evidence revealed that viruses may hijack the RNA replication mechanisms to facilitate virus production or eliminate the host immune system, demonstrating the role of viral infection-induced alternative splicing [61]. To examine the effect of SARS-CoV-2 infection on alternative splicing, we employed the detailed isoform RNA detection pipeline (Fig. 4**A**) to elucidate the genes with increased isoform levels in iPSC-AOs infected by SARS-CoV-2 (**Supplemental Table 2**). We employed the detailed isoform RNA detection pipeline (Fig. 4**A**) and summarized the genes with increased isoform levels (**Supplemental Table 2**). To analyze the biological roles of these genes with the most increased isoform levels, these genes were subjected to gene ontology analysis. Among these genes with highest isoform levels, the most enriched GO terms showed a high association with lipid metabolism, including sterol import (GO:0035376), cholesterol import (GO:0070508), regulation of very-low-density lipoprotein particle remodeling (GO:0010901), and regulation of lipoprotein lipase activity (GO:0051004) (Fig. 5**A**). As a threshold of 200 isoform counts, we found that 13 genes were detected for>200 counts, and 20 genes were<200 counts (Fig. 5**B**). According to the isoform counts, we tried to identify candidate genes with abundant isoform

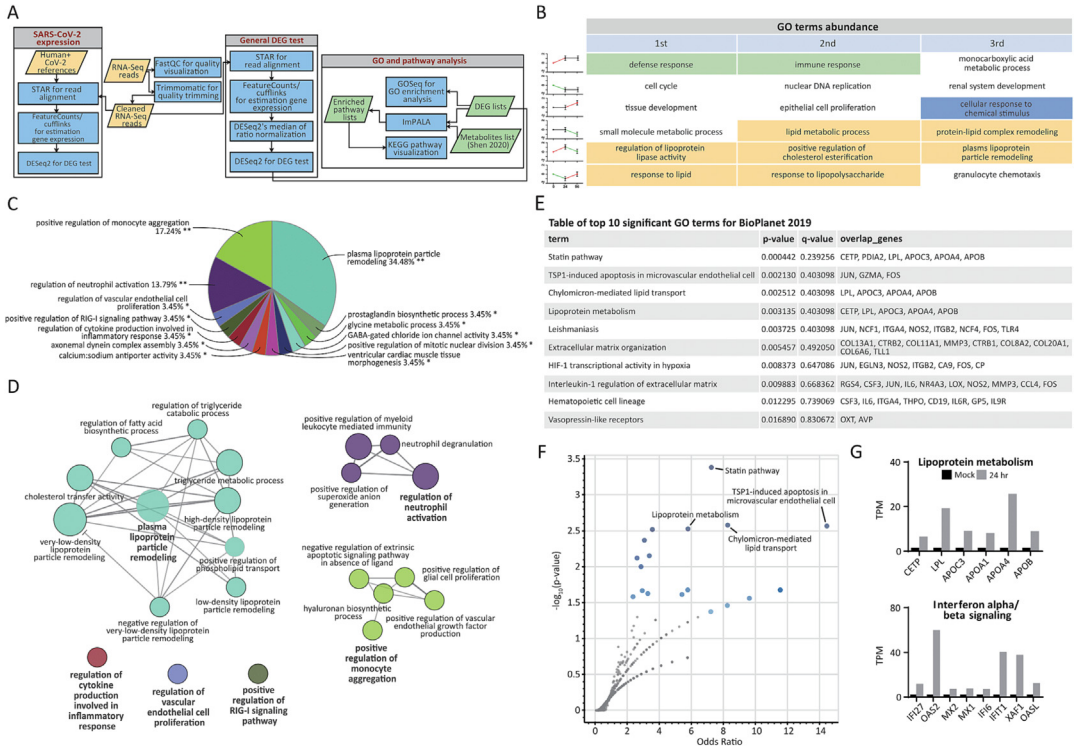

Fig. 4. Dysregulation of immune response and lipid biogenesis in airway organoids after SARS-CoV-2 infection. **(A)** The flowchart of gene ontology analysis. **(B)** Temporal DEGs were classified according to temporal dynamic patterns of gene expression at mock, 24 h, and 96 h samples. According to the expression from the RNA sequencing, we classified the pattern into five major patterns. In each pattern of gene expression, we examined the enrichment of the identified DEGs and list the three major activated biological processes. **(C)** ClueGO pathway analysis shows the overrepresented functional categories under SARS-CoV-2 infection (** $p < 0.001$, * $p < 0.01$). **(D)** The presentative GO terms were labeled in bold fonts. The bubble size reflects the frequency of the GO term in the underlying gene ontology annotation database. **(E)** The top 10 significant functions which were annotated by BioPlanet 2019 database. **(F)** The scattering plot of p-value vs. Odds Ratio of all DEGs after 24 h SARS-CoV-2 infection. **(G)** The transcript level of all associated genes of lipoprotein metabolism and interferon alpha/beta signaling from the RNA sequencing.

counts and significant fold change. After overlapping the genes with significant fold changes (>5 folds), five genes were obtained, including *DMBT1*, *RPS8*, *AC060780.1*, and *APOA1* (Fig. 5**C**). The mRNA levels of these five genes were highly upregulated at 24 h post-infection and then declined at 96 h post-infection (Fig. 5**D**). Among these genes, *APOA1* and *DMBT1* exhibited the most significant changes. *APOA1*, a constituent of high-density lipoprotein and a regulator responsible for cholesterol esterification, has been associated with the risk of SARS-CoV-2 infection [62]. *DMBT1* is a virus-scavenging protein that can modulate innate defense responses [63] and has been shown to be enriched in COVID-19 samples [64]. Sashimi plot showed the generation of two novel isoforms of *APOA1* and six isoforms of *DMBT1* in the iPSC-AOs at 24 h post-infection compared to uninfected iPSC-AOs (Fig. 5**E and 5F**). Collectively, our data using the iPSC-AO platform demonstrated that SARS-CoV-2 hijacked the RNA replication mechanisms and promoted ~~the~~ alternative splicing, leading to the generation of novel isoforms of *APOA1* and *DMBT1*. Considering the antiviral roles of *APOA1* [65] and *DMBT1* [66], the upregulation of *APOA1* and *DMBT1* may be the consequences of host self-defense in response to SARS-CoV-2 infection.

Modifications of lipid pathways restrict the internalization and replication of SARS-CoV-2

Along with the observations in bioinformatics analysis, our data suggested that SARS-CoV-2 modified the host lipid metabolism (Fig. 4) accompanied by the increase of *APOA1*, a regulator that contributes to cholesterol metabolism (Fig. 5). Lipids have been shown to play essential roles in the life cycle of viruses. Viral infection may interfere with ~~the~~ intracellular lipid metabolism, remodel the lipid composition of cell membranes, and generate new virions [17]. To test the critical roles of lipid metabolism during SARS-CoV-2 infection, we perturbed the lipid homeostasis using statin drugs and examined if this perturbation modified SARS-CoV-2 infection in iPSC-AOs. Prior to testing the effect of statins on iPSC-AOs infected with SARS-CoV-2, we evaluated whether the pretreatment of statin drugs affects the infection of ACE2-overexpressing HEK293T cells (HEK293-ACE2) by SARS-CoV-2 pseudovirus that expresses a luciferase reporter gene and SARS-CoV-2 S protein. First, treatment of statin drugs (i.e. Fluvastatin and Simvastatin) showed no cytotoxicity at any given dose in HEK293-ACE2 cells (**Supplemental Fig. 2**). We next treated HEK293-ACE2 cells with either Fluvastatin or Simvastatin for 24 h and subsequently evaluated the infection of SARS-CoV-2 pseudovirus by detecting the luciferase signals (**Supplemental Fig. 3**A). The entry of SARS-CoV-2 pseudovirus was moderately suppressed by the preincubation of either statin drug at 5 μM. The maximal inhibition of the entry of SARS-CoV-2 pseudovirus by both statins was achieved at 10 μM (**Supplemental Fig. 3**B), which was subjected to the following experiments. For the infection studies using SARS-CoV-2, iPSC-AOs were treated with statins for 24 h, followed by SARS-CoV-2 infection (MOI = 1) for another 24 h (Fig. 6**A**). The effect of Remdesivir, the well-established clinical drug for treating COVID-19 [67,68], was also evaluated in another parallel incubation of iPSC-AOs (**Supplemental Fig. 4**A). Immunoblotting and immunofluorescence showed that preincubation of Remdesivir reduced SARS-CoV-2 N protein expression in infected iPSC-AOs (**Supplemental Fig. 4**B & C), indicating the repression of SARS-CoV-2 replication by Remdesivir. Similar to

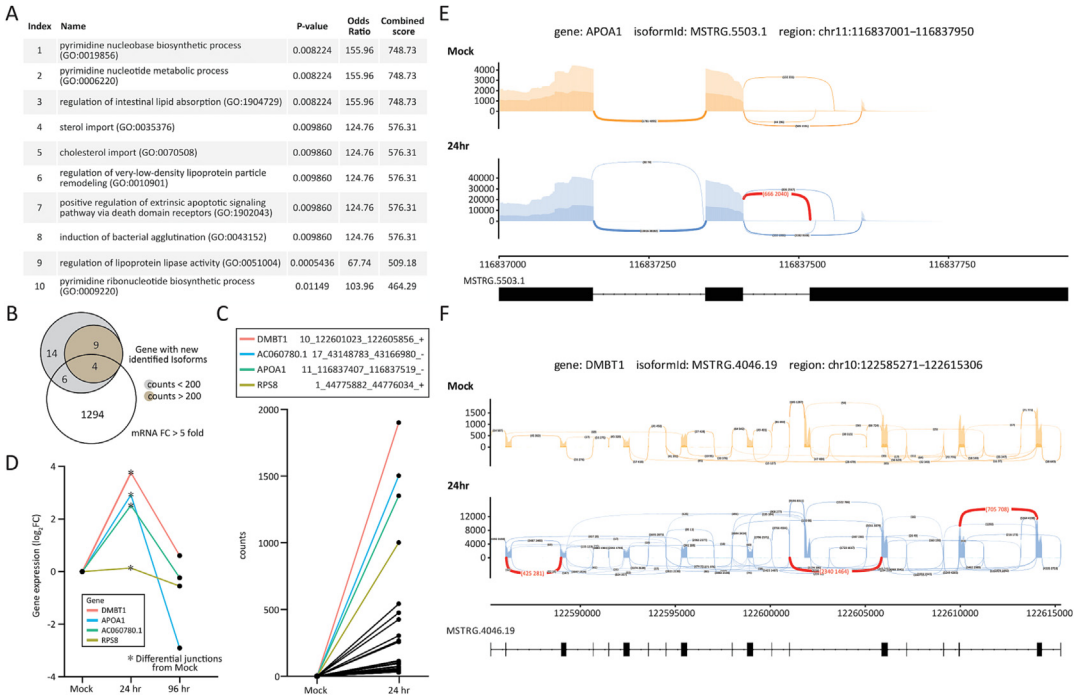

Fig. 5. Alternative splicing expression and junction analysis after SARS-CoV-2 infection. (A) the gene ontology of all upregulated genes with significantly upregulated isoform expression. **(B)** Venn's diagram showed the isoform lower than 200 counts (20 genes, isoform counts ⟨200) and higher than 200 counts (13 genes, isoform counts > 200). These isoforms intersected with the significantly upregulated genes (mRNA FC > 5 fold). **(C)** The transcript expression of identified isoform post SARS-CoV-2 infection. The information in the box showed the top ten genes with abundant isoform transcripts and their coordinates. **(D)** Differential spicing junction analysis identified new spicing isoforms. Differential expression spicing junction was found in five genes. *DMBT1*, *RPS8*, *AC060780.1*, and *APOA1* were found in a comparison of mock vs. 24 h. and HSPA5 was found in a comparison of mock vs. 96 h. Asterisk indicates the condition that differential expression spicing junction was found compared to the uninfected mock samples. **(E)** Sashimi plots of gene *APOA1*. This plot focuses on the human genome region chr11:116837001–116837950. An alternative splicing junction was discovered at the 24 h infected sample compared to the uninfected mock samples. The transformed expression levels at the two replicates of the 24 h infected samples in the splicing junctions are (666,2,040). **(F)** Sashimi plots of gene *DMBT1*. This plot focuses on the human genome region chr10:122585271–122615306. Three alternative splicing junctions were discovered at the 24 h infected sample compared to the uninfected mock samples. The transformed expression levels at the two replicates of the 24 h infected samples in the three splicing junctions are (425,281), (2,340,1,464), and (705,708), respectively.

the effect of Remdesivir, immunoblotting showed that preincubation of iPSC-AOs to statin drugs (i.e. Fluvastatin and Simvastatin, 10 μM) also substantially decreased the expression of N protein and TMPRSS2 in infected iPSC-AOs (Fig. 6**B**). Immunofluorescence further validated the effect of statins on N protein expression. The absence of N protein in infected iPSC-AOs preincubated with statins indicated that modifying lipid homeostasis repressed SARS-CoV-2 replication (Fig. 6**C**). To investigate whether statin pretreatment modified SARS-CoV-2 entry, we examined the effect of statins on ACE2 trafficking in HEK293-ACE2 cells using immunofluorescence. Upon the treatment of both statins in HEK293-ACE2 cells, we observed a dose-dependent internalization of ACE2 from the cell membrane to the cytoplasm (Fig. 6**D & 6E**). SARS-CoV-2 as one of the positive-sense single-stranded RNA viruses has been known to exhibit a high-frequency mutation rate. In addition to the Wuhan variant, other variants were also consecutively identified. Among them, the Omicron variant as the most recently identified SARAS-CoV-2 variant has been reported to be a more aggressive and dominant strain globally [2]. To further examine whether statin treatment also hinders the viral entry of SARS-CoV-2, we subjected statin-pretreated HEK293-ACE2 cells to the viral infection using four different SARS-CoV-2 pseudoviruses that express a luciferase reporter protein and the S protein derived from various SARS-CoV-2 variants, including wild-type, alpha, delta, and omicron. The amino difference in the spike protein among Wuhan, Alpha, Delta, and Omicron variants used for the SARS-CoV-2 pseudovirus generation are shown in Fig. 6**F**. Compared with the wild-type Wuhan variant, the amino acid differences were depicted with triangle symbols (Fig. 6**F**). As detected by the luciferase assay, both statin drugs (Fluvastatin and Simvastatin, 10 μM) consistently abrogated the entry of SARS-CoV-2 pseudoviruses with the S proteins of different SARS-CoV-2 strains (Fig. 6**G**). Collectively, our data demonstrated that interfering the lipid homeostasis with statin drugs restricts the entry and replication of SARS-CoV-2 in the host cells.

Discussion

The rapid spread and persistence of the COVID-19 pandemic have brought a great threat to the economy and public health system in the world. Investigators and clinicians have made several efforts to develop novel strategies or technologies for treating COVID-19 [1]. Despite the anti-pandemic measures and achievements, including novel therapeutics, the rapid development of vaccines, and the high vaccination coverage, the pandemic still remains poorly controlled. The difficulty in the pandemic control against COVID-19 was partially attributed to the verification of several SARS-COV-2 variants, including the Wuhan variant, Alpha variant, Delta variant, and Omicron variant [2]. Although virus-inhibiting drugs, such as Paxlovid, Molnupiravir, and Remdesivir, have shown efficacy in viral clearance among COVID-19 patients [69], more efforts are still required to combat the viral infection by emerging variants of SARS-CoV-2. Notably, COVID-19 patients with pre-existing metabolic conditions are associated with higher hospitalization and mortality [70]. On the contrary, modulations of aberrant lipid metabolism are linked to lower disease morbidity and mortality in COVID-19 patients [14–16 17]. Collectively, these

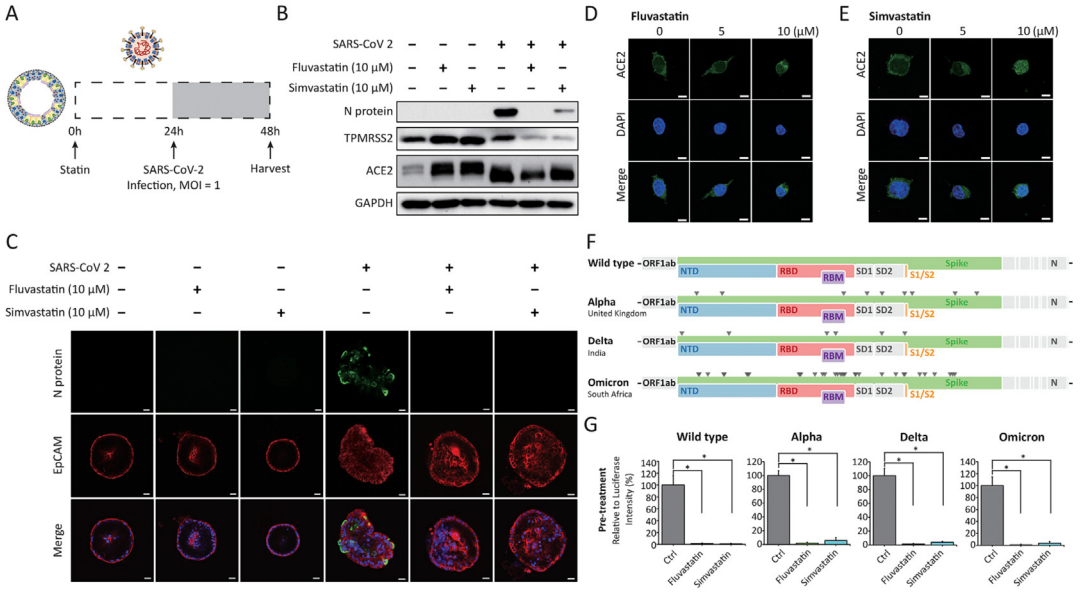

Fig. 6. Statin alters ACE2 localization in SARS-CoV-2 infected airway organoids. (A) The scheme of Statin analogs treatment to the SARS-CoV-2 infected AO. (B) We used immunoblotting analysis and (C) immunofluorescence staining to assay the inhibition effect on the N protein production in SARS-CoV-2-infected AO after 10 μM Fluvastatin or Simvastatin treatment. We detected the ACE2, TMPRSS2, and N protein levels in the indicated viruses/Statin combinations. GAPDH protein was used as a loading control. Immunofluorescence staining of N protein in the AO. The AO cells were stained for N protein (green) or EpCAM (red) and counterstained with DAPI (blue). Scale bar = 10 μm. (D, E) We used immunofluorescence staining to trace the ACE2 internalization process after indicated concentration of Fluvastatin or Simvastatin treatment. The airway organoid cells were stained for ACE2 (green) and counterstained with DAPI (blue). Scale bar = 10 μm. (F) Geographical drawing of amino acid changes in the spike protein of Wuhan, Alpha, Delta, and Omicron SARS-CoV-2 variants. The differences are shown in reference to SARS-CoV-2 Wuhan-1 genome, labeled with triangle. NTD, N-terminal domain; RBD, receptor binding domain; RBM, receptor binding motif; SD1, subdomain 1; SD2, subdomain 2; N, nucleocapsid. (G) Luciferase assay for quantification of SARS-CoV-2 pseudovirus infection (one MOI) in the 10 μM Fluvastatin or Simvastatin treated HEK293-ACE2 cells. Until 48 h later, we harvested the cell lysate for detecting the luciferase activity. The luciferase activity of each sample was normalized to the untreated control as 100%. Significance was determined by two-way ANOVA (*, $p < 0.001$). (For interpretation of the references to colour in this figure legend, the reader is referred to the web version of this article.)

observations suggested that the regulation of lipid pathways serves certain roles that are critical but unclear in the pathogenesis of SARS-CoV-2 infection.

The high infectivity of SARS-CoV-2 was considered a factor that largely hindered the conduction of the virology research on COVID-19. In addition to the requirement of ~~a~~ biosafety level 3 (BSL-3) laboratory facilities, experimental platforms mimicking SARS-CoV-2 infection in the human body are also essential. Syrian golden hamsters exhibit pathological changes similar to that in COVID-19 patients and are therefore widely used as the *in vivo* model to examine the efficacy of vaccines and therapeutics [71–73]. However, Syrian golden hamsters exhibit no lethality in response to SARS-CoV-2 infection. Instead, the major post-infection phenotype of this model is mild weight loss which is spontaneously recovered within two weeks [71]. The discrepancy between the phenotypes of this model and the clinical manifestations of COVID-19 pointed out the limitations of Syrian golden hamsters as a COVID-19 model due to the species difference. *In vitro* models using cells derived from the human lung may compensate for the gap between animal models and COVID-19 patients and provide further understanding of the pathological mechanisms of this critical infectious disease. Immortalized human cell lines are powerful and easy to be handled whereas it is unclear whether ~~the~~ normal respiratory physiology is maintained in these cells. Primary human cells are competent to provide better information that is biologically relevant and patient-specific, rendering their advantages over immortalized cells. Nevertheless, the availability of primary human cells is usually limited and hindered their utility for high throughput studies [74]. The development of iPSC technologies and organoid-based research have largely relieved these aforementioned concerns. iPSCs are self-renewing and can expand unlimitedly. After defined differentiation, iPSC-derived organoids are patient-specific and readily to be cultured and used in translational research [10,75]. In the present study, we generated iPSC-AOs that carry high availability and cell heterogeneity similar to the human native airway. Using scRNAseq-based approaches, we found several distinct cell clusters within the iPSC-AOs, including the basal cells, secretory cells, and multiciliated cells. In addition to the similarity of unique gene expression at the single cell level, iPSC-AOs also showed microstructures resembling that in the human native airway (Fig. 1). Along with identifying the expression of ACE2 (Fig. 2), our data supported the 3D iPSC-AOs as an ideal platform that is physiologically relevant and feasible for SARS-CoV-2 infection studies.

Bioinformatics analysis demonstrated the involvement of dysregulated lipid pathways in SARS-CoV-2-infected iPSC-AOs (Figs. 3 and 4). In addition, SARS-CoV-2 hijacked the RNA replication machinery in the host cells and promoted the alternative splicing (Fig. 5). During the splicing processes, the host cells generated novel isoforms of two genes, i.e. *APOA1* and *DMBT1*, which may exert functions associated with cholesterol esterification, virus scavenging, or antiviral activity. Without regard to the possible roles of these genes in self-defense in the host cells, our findings of bioinformatics approaches clearly demonstrated the enrichment of numerous lipid pathways in infected iPSC-AOs. To test the role of lipid pathways in SARS-CoV-2 infection in iPSC-AOs, we modified the lipid homeostasis in uninfected host cells by incubating with the cholesterol-lowering drug statins, including iPSC-AOs and ACE2-overexpressing HEK293T cells, before the exposures to SARS-CoV-2 or luciferase-expressing SARS-CoV-2 pseudoviruses. Evidenced by the decrease in incorporated luciferase signals, modifying the lipid homeostasis using statins decreased the viral entry of SARS-CoV-2 pseudoviruses containing the S proteins from different SARS-CoV-2 variants (**Supplemental Fig. 3**A and **Supplemental Fig. 6**G). Meanwhile, statins promoted the internalization of ACE2 protein from the cell membrane to the cytoplasm in a

dose-dependent manner (Fig. 6**D and 6E**). These data indicated that modifications of lipid homeostasis using statins reduced SARS-CoV-2 pseudovirus entry through the relocation of ACE2, the entry receptor for SARS-CoV-2. The same treatment also largely reduced the SARS-CoV-2 N protein in SARS-CoV-2-infected iPSC-AOs (Fig. 6**B and 6C**), indicating that interference of lipid homeostasis also suppressed SARS-CoV-2 replication within the host cells. Our findings supported the previous clinical observations of the association of prognosis with preexisting metabolic abnormalities [70] or the use of lipid-modifying drugs among COVID-19 patients [14–16 17].

Despite the beneficial effects of lipid modifications in suppressing SARS-CoV-2 entry and replication, it remains questionable whether lipid-modifying drugs can be used as anti-viral medications in COVID-19 patients. In the present study, we examined the pretreatment effect of lipid modifications on SARS-CoV-2 entry and replication. However, post-infection treatment of the same drugs did not decrease the viral loads in SARS-CoV-2-infected iPSC-AOs (**data not shown**). Our observations only showed the efficacy of lipid modifications in pretreatment studies rather than post-treatment studies. It remains ambiguous whether the efficacy of statin drugs on SARS-CoV-2 infection was exerted through the Statin-mediated cholesterol reduction or direct Statin-ACE2 interaction. Further studies will be required to elucidate the mechanisms underlying Statin-mediated ACE2 trafficking. SARS-CoV2 enters the mammalian cells and uses the host machinery of replicate themselves to cause infection. After the replication and the damage of host cells, SARS-CoV-2 may induce secondary infection and further exacerbate the damage. As shown in our findings, lipid modifications using Statins at least led to prominent inhibition of SARS-CoV-2 entry, which may subsequently prevent the viral replication within the cells, eventually rescuing the host cells from virus-induced apoptotic death. Interestingly, the fatty acid synthesis inhibitor orlistat was shown to block SARS-CoV-2 replication [76]. Targeting the metabolism of lipids (e.g. cholesterol and sphingolipids) also exhibited therapeutic efficacy in the host cells infected by flaviviruses [57] or hepatitis C virus [77]. The evidences reported by previous studies also supported that cholesterol and sphingolipids, the constituents of lipid rafts", serve certain roles crucial for viral infection in the host cells.

Conclusion

Collectively, our findings have demonstrated evidence showing that modifications of lipid pathways using Statin drugs effectively suppressed SARS-CoV-2 infection in iPSC-AOs. The beneficial effect of Statin was, at least, partially through the relocation of ACE2 from the cell membrane to the cytosol, which hindered the viruses to enter and propagate within the host cells. SARS-CoV-2 as one of the RNA viruses has been well known to carry a high probability of mutations in the virions, leading to the frequent development of drug resistance against anti-viral drugs. Targeting ~~to~~ certain host factors such as the metabolisms of cholesterol or other lipids may represent alternative approaches against SARS-CoV-2 infection. The combination of interferon and sphingolipid synthesis inhibitor was used to treat hepatitis C virus infection [77]. Reduction in cholesterol levels increased interferon responses to suppress the infection of Dengue and Zika viruses [57]. These observations highlighted that the intervention targeting lipid pathways can be combined with conventional antiviral drugs (such as Remdesivir, etc) and used as a combination therapy to combat the long-lasting COVID-19 pandemic. However, more pre-clinical and clinical data are still needed to verify this speculation.

Ethics approval and consent to participate

This study was approved by the ethics committee (committee's reference number, AS-IRB01-21038).

CRediT authorship contribution statement

Ping-Hsing Tsai: Conceptualization. **Yueh Chien:** Writing – review & editing. **Man Sheung Chan:** Methodology. **Winnie Khor:** Writing - original draft. **Yi-Ying Lin:** Validation. **Chih-Ling Yeh:** Visualization. **Mong-Lien Wang:** Writing - original draft. **Yi-Ping Yang:** Data curation. **Fu-Ting Tsai:** Investigation. **Meng-Shiue Lee:** Data curation. **Shan-Ko Tsai:** Validation. **Ping-Cheng Liu:** Investigation. **Shih-Jie Chou:** Supervision. **Shih-Hwa Chiou:** Supervision.

Declaration of Competing Interest

The authors declare that they have no known competing financial interests or personal relationships that could have appeared to influence the work reported in this paper.

Acknowledgement

The authors would like to thank Miss Yi-Ching Tsai, Yu-Ling Ko, and Mr. Ming-Long Tsai for their support in the study. In addition, we thank Shih-Yu Chen and Sung-Lin Tsai for useful discussion on statistical analysis. This work was supported by the National Science and Technology Council [NSTC 111-2320-B-075-008, 111-2320-B-075-007, 111-2321-B-A49-009, 111-2320-B-A49-028-MY3, 112-2321-B-A49-007], Taipei Veterans General Hospital [V111B-015, V111B-022, V111B-025, 111VACS-003, 111VACS-007], Yen Tjing Ling Medical Foundation (CI-111-23), and VGH, TSGH, AS Joint Research Program (AS-VTA-111-07), Ministry of Economic Affairs, R.O.C. (112-EC-17-A-20-S6-026. This work was financially supported by the "Center for Intelligent Drug Systems and Smart Bio-devices (IDS2B)" from The Featured Areas Research Center Program within the framework of the Higher Education Sprout Project by the Ministry of Education (MOE) in Taiwan.

Appendix A. Supplementary data

Supplementary data to this article can be found online at https://doi.org/10.1016/j.jare.2023.08.005.

References

[1] Rahman S, Montero MTV, Rowe K, Kirton R, Kunik Jr F. Epidemiology, pathogenesis, clinical presentations, diagnosis and treatment of COVID-19: A review of current evidence. Expert Rev Clin Pharmacol 2021;14(5):601–21.
[2] Tian D, Sun Y, Xu H, Ye Q. The emergence and epidemic characteristics of the highly mutated SARS-CoV-2 Omicron variant. J Med Virol 2022;94(6):2376–83.
[3] Takahashi K, Tanabe K, Ohnuki M, Narita M, Ichisaka T, Tomoda K, et al. Induction of pluripotent stem cells from adult human fibroblasts by defined factors. Cell 2007;131(5):861–72.
[4] Watanabe M, Buth JE, Vishlaghi N, de la Torre-Ubieta L, Taxidis J, Khakh BS, et al. Self-organized cerebral organoids with human-specific features predict effective drugs to combat zika virus infection. Cell Rep 2017;21(2):517–32.
[5] Sato T, Vries RG, Snippert HJ, van de Wetering M, Barker N, Stange DE, et al. Single Lgr5 stem cells build crypt-villus structures in vitro without a mesenchymal niche. Nature 2009;459(7244):262–5.
[6] Gorkhali R, Koirala P, Rijal S, Mainali A, Baral A, Bhattarai HK. Structure and function of major SARS-CoV-2 and SARS-CoV proteins. Bioinform Biol Insights 2021;15. 11779322211025876.
[7] Lamers MM, van der Vaart J, Knoops K, Riesebosch S, Breugem TI, Mykytyn AZ, et al. An organoid-derived bronchioalveolar model for SARS-CoV-2 infection of human alveolar type II-like cells. EMBO J 2021;40(5):e105912.

[8] Tindle C, Fuller M, Fonseca A, Taheri S, Ibeawuchi SR, Beutler N, et al. Adult stem cell-derived complete lung organoid models emulate lung disease in COVID-19. Elife 2021:10.
[9] Han Y, Duan X, Yang L, Nilsson-Payant BE, Wang P, Duan F, et al. Identification of SARS-CoV-2 inhibitors using lung and colonic organoids. Nature 2021;589 (7841):270–5.
[10] Ahmad Mulyadi Lai HI, Chou S-J, Chien Y, Tsai P-H, Chien C-S, Hsu C-C, et al. Expression of endogenous angiotensin-converting enzyme 2 in human induced pluripotent stem cell-derived retinal organoids. Int J Mol Sci 2021;22(3):1320.
[11] Spitalieri P, Centofanti F, Murdocca M, Scioli MG, Latini A, Di Cesare S, et al. Two different therapeutic approaches for SARS-CoV-2 in hiPSCs-derived lung organoids. Cells 2022;11(7):1235.
[12] Wang C, Zhang M, Garcia G, Jr., Tian E, Cui Q, Chen X, et al. ApoE-Isoform-Dependent SARS-CoV-2 Neurotropism and Cellular Response. Cell Stem Cell. 2021;28(2):331-42 e5.
[13] Bose B, Kapoor S, Nihad M. Induced pluripotent stem cell derived human lung organoids to map and treat the SARS-CoV2 infections in vitro. Advances in Experimental Medicine and Biology 2021;1312:1–17.
[14] Rodriguez-Nava G, Trelles-Garcia DP, Yanez-Bello MA, Chung CW, Trelles-Garcia VP, Friedman HJ. Atorvastatin associated with decreased hazard for death in COVID-19 patients admitted to an ICU: a retrospective cohort study. Crit Care 2020;24(1):429.
[15] Tan WYT, Young BE, Lye DC, Chew DEK, Dalan R. Statin use is associated with lower disease severity in COVID-19 infection. Sci Rep 2020;10(1):17458.
[16] Bifulco M, Ciccarelli M, Bruzzese D, Dipasquale A, Lania AG, Mazziotti G, et al. The benefit of statins in SARS-CoV-2 patients: further metabolic and prospective clinical studies are needed. Endocrine 2021;71(2):270–2.
[17] Theken KN, Tang SY, Sengupta S, FitzGerald GA. The roles of lipids in SARS-CoV-2 viral replication and the host immune response. J Lipid Res 2021;62:100129.
[18] Huang K-Y, Lin M-S, Kuo T-C, Chen C-L, Lin C-C, Chou Y-C, et al. Humanized COVID-19 decoy antibody effectively blocks viral entry and prevents SARS-CoV-2 infection. EMBO Mol Med 2021;13(1):e12828.
[19] McCauley KB, Hawkins F, Kotton DN. Derivation of epithelial-only airway organoids from human pluripotent stem cells. Curr Protoc Stem Cell Biol 2018;45(1):e51.
[20] Tsai P-H, Chien Y, Wang M-L, Hsu C-H, Laurent B, Chou S-J, et al. Ash2l interacts with Oct4-stemness circuitry to promote super-enhancer-driven pluripotency network. Nucleic Acids Res 2019;47(19):10115–33.
[21] Andrews S. FastQC: A Quality Control Tool for High Throughput Sequence Data [Online]. 2010 [.
[22] Sewe SO, Silva G, Sicat P, Seal SE, Visendi P. Trimming and validation of illumina short reads using trimmomatic, trinity assembly, and assessment of RNA-Seq data. Methods Mol Biol 2022;2443:211–32.
[23] Dobin A, Davis CA, Schlesinger F, Drenkow J, Zaleski C, Jha S, et al. STAR: Ultrafast universal RNA-seq aligner. Bioinformatics 2013;29(1):15–21.
[24] Kim D, Lee JY, Yang JS, Kim JW, Kim VN, Chang H. The Architecture of SARS-CoV-2 Transcriptome. Cell 2020;181(4):914–21 e10.
[25] Wyler E, Mösbauer K, Franke V, Diag A, Gottula LT, Arsiè R, et al. Transcriptomic profiling of SARS-CoV-2 infected human cell lines identifies HSP90 as target for COVID-19 therapy. iScience 2021;24(3):102151.
[26] Liao Y, Smyth GK, Shi W. FeatureCounts: An efficient general purpose program for assigning sequence reads to genomic features. Bioinformatics 2014;30 (7):923–30.
[27] Love MI, Huber W, Anders S. Moderated estimation of fold change and dispersion for RNA-seq data with DESeq2. Genome Biol 2014;15(12):550.
[28] Wickham H. ggplot2: Elegant Graphics for Data Analysis. New York: Springer-Verlag; 2016.
[29] Wu H-M, Tien Y-J, Chen C-H. GAP: A graphical environment for matrix visualization and cluster analysis. Comput Stat Data Anal 2010;54(3):767–78.
[30] Ashburner M, Ball CA, Blake JA, Botstein D, Butler H, Cherry JM, et al. Gene ontology: Tool for the unification of biology. The Gene Ontology Consortium Nat Genet 2000;25(1):25–9.
[31] Gene OC. The Gene Ontology resource: Enriching a GOld mine. Nucleic Acids Res 2021;49(D1):D325–34.
[32] Young MD, Wakefield MJ, Smyth GK, Oshlack A. Gene ontology analysis for RNA-seq: Accounting for selection bias. Genome Biol 2010;11(2):R14.
[33] Sayols S. rrvgo: a Bioconductor package to reduce and visualize Gene Ontology terms. 2020.
[34] Supek F, Bošnjak M, Škunca N, Šmuc T, Gibas C. REVIGO summarizes and visualizes long lists of gene ontology terms. PLoS One 2011;6(7):e21800.
[35] Almende B.V.et al. visNetwork: Network Visualization using 'vis.js' Library. R package version 2.1.0. 2021.
[36] Shen B, Yi X, Sun Y, Bi X, Du J, Zhang C, et al. Proteomic and Metabolomic Characterization of COVID-19 Patient Sera. Cell 2020;182(1):59–72 e15.
[37] Kamburov A, Cavill R, Ebbels TM, Herwig R, Keun HC. Integrated pathway-level analysis of transcriptomics and metabolomics data with IMPaLA. Bioinformatics 2011;27(20):2917–8.
[38] Kuleshov MV, Jones MR, Rouillard AD, Fernandez NF, Duan Q, Wang Z, et al. Enrichr: A comprehensive gene set enrichment analysis web server 2016 update. Nucleic Acids Res 2016;44(W1):W90–7.
[39] Bindea G, Mlecnik B, Hackl H, Charoentong P, Tosolini M, Kirilovsky A, et al. ClueGO: a Cytoscape plug-in to decipher functionally grouped gene ontology and pathway annotation networks. Bioinformatics 2009;25(8):1091–3.
[40] Kim D, Paggi JM, Park C, Bennett C, Salzberg SL. Graph-based genome alignment and genotyping with HISAT2 and HISAT-genotype. Nat Biotechnol 2019;37(8):907–15.
[41] Pertea M, Kim D, Pertea GM, Leek JT, Salzberg SL. Transcript-level expression analysis of RNA-seq experiments with HISAT. StringTie and Ballgown Nat Protoc 2016;11(9):1650–67.
[42] Feng Y-Y, Ramu A, Cotto KC, Skidmore ZL, Kunisaki J, Conrad DF, et al. RegTools: Integrated analysis of genomic and transcriptomic data for discovery of splicing variants in cancer. bioRxiv 2018.
[43] Pertea M, Pertea GM, Antonescu CM, Chang TC, Mendell JT, Salzberg SL. StringTie enables improved reconstruction of a transcriptome from RNA-seq reads. Nat Biotechnol 2015;33(3):290–5.
[44] Fu J, Frazee AC, Collado-Torres L, Jaffe AE, Leek JT. ballgown: Flexible, isoform-level differential expression analysis. 2021.
[45] Vitting-Seerup K, Sandelin A. The landscape of isoform switches in human cancers. Mol Cancer Res. 2017;15(9):1206–20.
[46] Vitting-Seerup K, Sandelin A. IsoformSwitchAnalyzeR: analysis of changes in genome-wide patterns of alternative splicing and its functional consequences. Bioinformatics. 2019;35(21):4469-71.
[47] Garrido-Martín D, Palumbo E, Guigó R, Breschi A, Pertea M. ggsashimi: Sashimi plot revised for browser- and annotation-independent splicing visualization. PLoS Comput Biol 2018;14(8):e1006360.
[48] Travaglini KJ, Nabhan AN, Penland L, Sinha R, Gillich A, Sit RV, et al. A molecular cell atlas of the human lung from single-cell RNA sequencing. Nature 2020;587(7835):619–25.
[49] Xiaojun W, Yan L, Hong X, Xianghong Z, Shifeng L, Dingjie X, et al. Acetylated alpha-tubulin regulated by N-Acetyl-Seryl-Aspartyl-Lysyl-Proline(Ac-SDKP) exerts the anti-fibrotic effect in rat lung fibrosis induced by silica. Sci Rep 2016;6:32257.
[50] Walls AC, Park YJ, Tortorici MA, Wall A, McGuire AT, Veesler D. Structure, function, and antigenicity of the SARS-CoV-2 spike glycoprotein. Cell 2020;181 (2):281–92 e6.
[51] Letko M, Marzi A, Munster V. Functional assessment of cell entry and receptor usage for SARS-CoV-2 and other lineage B betacoronaviruses. Nat Microbiol 2020;5(4):562–9.
[52] Gutiérrez-Chamorro L, Riveira-Muñoz E, Barrios C, Palau V, Nevot M, Pedreño-López S, et al. SARS-CoV-2 infection modulates ACE2 function and subsequent inflammatory responses in swabs and plasma of COVID-19 patients. Viruses 2021;13(9):1715.
[53] Cicco S, Cicco G, Racanelli V, Vacca A. Neutrophil extracellular traps (NETs) and damage-associated molecular patterns (DAMPs): Two potential targets for COVID-19 treatment. Mediators Inflamm 2020;2020:1–25.
[54] Land WG. Role of DAMPs in respiratory virus-induced acute respiratory distress syndrome-with a preliminary reference to SARS-CoV-2 pneumonia. Genes Immun 2021;22(3):141–60.
[55] Kozlov EM, Ivanova E, Grechko AV, Wu W-K, Starodubova AV, Orekhov AN. Involvement of oxidative stress and the innate immune system in SARS-CoV-2 infection. Diseases 2021;9(1):17.
[56] Read SA, Douglas MW. Virus induced inflammation and cancer development. Cancer Lett 2014;345(2):174–81.
[57] Osuna-Ramos JF, Reyes-Ruiz JM, Del Angel RM. The role of host cholesterol during flavivirus infection. Front Cell Infect Microbiol 2018;8:388.
[58] Wang ET, Sandberg R, Luo S, Khrebtukova I, Zhang Lu, Mayr C, et al. Alternative isoform regulation in human tissue transcriptomes. Nature 2008;456 (7221):470–6.
[59] Zhu Na, Zhang D, Wang W, Li X, Yang Bo, Song J, et al. A novel coronavirus from patients with pneumonia in china, 2019. N Engl J Med 2020;382(8):727–33.
[60] Wang C, Chen L, Chen Y, Jia W, Cai X, Liu Y, et al. Abnormal global alternative RNA splicing in COVID-19 patients. PLoS Genet 2022;18(4):e1010137.
[61] Chauhan K, Kalam H, Dutt R, Kumar D. RNA splicing: A new paradigm in host-pathogen interactions. J Mol Biol 2019;431(8):1565–75.
[62] Hilser JR, Han Yi, Biswas S, Gukasyan J, Cai Z, Zhu R, et al. Association of serum HDL-cholesterol and apolipoprotein A1 levels with risk of severe SARS-CoV-2 infection. J Lipid Res 2021;62:100061.
[63] Ligtenberg AJ, Karlsson NG, Veerman EC. Deleted in malignant brain tumors-1 protein (DMBT1): A pattern recognition receptor with multiple binding sites. Int J Mol Sci 2010;11(12):5212–33.
[64] Park J, Foox J, Hether T, Danko D, Warren S, Kim Y, et al. Systemic tissue and cellular disruption from SARS-CoV-2 infection revealed in COVID-19 autopsies and spatial omics tissue maps. bioRxiv. 2021.
[65] Srinivas RV, Birkedal B, Owens RJ, Anantharamaiah GM, Segrest JP, Compans RW. Antiviral effects of apolipoprotein A-I and its synthetic amphipathic peptide analogs. Virology 1990;176(1):48–57.
[66] Zarei M, Bose D, Ali Akbari Ghavimi S, Nouri-Vaskeh M, Mohammadi M, Sahebkar A. Potential role of glycoprotein 340 in milder SARS-CoV-2 infection in children. Expert Rev Anti Infect Ther 2021;19(6):675–7.
[67] Beigel JH, Tomashek KM, Dodd LE, Mehta AK, Zingman BS, Kalil AC, et al. Remdesivir for the treatment of covid-19 - Final report. N Engl J Med 2020;383 (19):1813–26.
[68] Kokic G, Hillen HS, Tegunov D, Dienemann C, Seitz F, Schmitzova J, et al. Mechanism of SARS-CoV-2 polymerase stalling by remdesivir. Nat Commun 2021;12(1).
[69] Zou R, Peng L, Shu D, Zhao L, Lan J, Tan G, et al. Antiviral efficacy and safety of molnupiravir against omicron variant infection: A randomized controlled clinical trial. Front Pharmacol 2022;13:939573.

[70] Denson JL, Gillet AS, Zu Y, Brown M, Pham T, Yoshida Y, et al. Metabolic syndrome and acute respiratory distress syndrome in hospitalized patients With COVID-19. JAMA Netw Open 2021;4(12):e2140568.
[71] Imai M, Iwatsuki-Horimoto K, Hatta M, Loeber S, Halfmann PJ, Nakajima N, et al. Syrian hamsters as a small animal model for SARS-CoV-2 infection and countermeasure development. Proceedings of the National Academy of Sciences of the United States of America 2020;117(28):16587–95.
[72] Baum A, Ajithdoss D, Copin R, Zhou A, Lanza K, Negron N, et al. REGN-COV2 antibodies prevent and treat SARS-CoV-2 infection in rhesus macaques and hamsters. Science 2020;370(6520):1110–5.
[73] Imbrechts M, Maes W, Ampofo L, Van den Berghe N, Calcoen B, Van Looveren D, et al. Potent neutralizing anti-SARS-CoV-2 human antibodies cure infection with SARS-CoV-2 variants in hamster model. iScience 2022;25(8):104705.
[74] Miller AJ, Spence JR. In vitro models to study human lung development. Disease and Homeostasis Physiology (Bethesda) 2017;32(3):246–60.
[75] Huang K-C, Wang M-L, Chen S-J, Kuo J-C, Wang W-J, Nhi Nguyen PN, et al. Morphological and molecular defects in human three-dimensional retinal organoid model of X-linked juvenile retinoschisis. Stem Cell Rep 2019;13 (5):906–23.
[76] Chu J, Xing C, Du Y, Duan T, Liu S, Zhang P, et al. Pharmacological inhibition of fatty acid synthesis blocks SARS-CoV-2 replication. Nat Metab 2021;3 (11):1466–75.
[77] Amemiya F, Maekawa S, Itakura Y, Kanayama A, Matsui A, Takano S, et al. Targeting lipid metabolism in the treatment of hepatitis C virus infection. J Infect Dis 2008;197(3):361–70.
[78] Wang J-T, Lin Y-Y, Chang S-Y, Yeh S-H, Hu B-H, Chen P-J, et al. The role of phylogenetic analysis in clarifying the infection source of a COVID-19 patient. J Infect 2020;81(1):147–78.
[79] Kanehisa M. Toward understanding the origin and evolution of cellular organisms. Protein Sci 2019;28(11):1947–51.
[80] Kanehisa M, Furumichi M, Sato Y, Ishiguro-Watanabe M, Tanabe M. KEGG: Integrating viruses and cellular organisms. Nucleic Acids Res 2021;49(D1): D545–51.
[81] Kanehisa M, Goto S. KEGG: Kyoto encyclopedia of genes and genomes. Nucleic Acids Res 2000;28(1):27–30.
[82] Luo W, Brouwer C. Pathview: An R/Bioconductor package for pathway-based data integration and visualization. Bioinformatics 2013;29(14):1830–1.